Zwitterionic Hydrogel-Impregnated Membranes with Polyamide Skin Achieving Superior Water/Salt Separation Properties

Thien Tran,[1] Shiwei Pan[1,2], Xiaoyi Chen[1], Xiao-Ci Lin[1], Adrienne K. Blevins[3], Yifu Ding[3], and Haiqing Lin[1,*]

[1] Department of Chemical and Biological Engineering, University at Buffalo, The State University of New York, Buffalo, NY 14260, USA.

[2] Wanhua Chemical Group Co., Ltd., Economic Development Zone, Yantai, Shandong 264006, China.

[3] Materials Science and Engineering Program and Department of Mechanical Engineering, University of Colorado, Boulder, CO 80309, USA.

[*] Corresponding author. Tel: +1-716-645-1856, Email: haiqingl@buffalo.edu (H. Lin)

Revised submission to *ACS Applied Materials and Interfaces*

ABSTRACT

Support-free nonporous membranes have emerged as a new material platform for osmotic pressure-driven processes due to its insusceptibility to internal concentration polarization (ICP). Herein, we demonstrate high-performance membranes of zwitterionic hydrogels impregnated in porous membranes with a skin layer of highly cross-linked polyamides on both sides prepared by gel-liquid interfacial polymerization (GLIP). Such a configuration eliminates the pores and thus ICP, while the thin polyamide layer provides high salt rejection but negligible resistance to the water transport compared with the hydrogels. The polyamide skin layers are characterized using scanning electron microscopy and atomic force microscopy. The effect of the hydrogel compositions and polyamide formation conditions on the water/salt separation properties is thoroughly investigated. Example membranes show water permeance and salt rejection comparable to state-of-the-art commercial forward osmosis membranes and essentially no ICP.

KEYWORDS: Forward osmosis membranes; zwitterionic hydrogels; polyamides; water/salt separation; interfacial polymerization

1. INTRODUCTION

Osmotic pressure-driven membrane processes have attracted significant interests for desalination, wastewater treatment, food dewatering, and sustainable power generation.[1-5] When exposed to feed water with lower osmotic pressure on one side and a draw solution with higher osmotic pressure on the other side, the membrane selectively permeates water from the feed to the draw solution and retains other solutes in their corresponding sides. The key to these processes is membranes with high water permeance and high rejection of solutes (that provide osmotic pressure and driving force for water permeation).

Conventional membranes for osmotic pressure-driven processes are asymmetric cellulose acetate and polyamide-based thin-film composite (TFC) membranes, which comprise a thin selective layer with excellent water/salt separation properties and a porous substrate providing mechanical support for membrane handling and operation. However, the porous substrate poses two challenges. First, it causes internal concentration polarization (ICP), preventing a well-mixing of the permeated water and draw solution (if the substrate is faced with the draw solution) and lowering the effective osmotic pressure difference across the selective layer as shown in Figure 1a.[6, 7] For example, water flux of a polyamide-based TFC membrane (SW30-XLE) decreased by 97% due to the ICP.[7, 8] Second, the foulants (such as organic matters) can accumulate inside the porous substrate (*i.e.*, fouling), which aggravates the ICP and further decreases the water flux through the membrane.[9-11]

Development of membranes without the severe effect of the ICP has been identified as a key step to enabling the osmotic-pressure driven processes, such as forward osmosis (FO), pressure-retarded osmosis (PRO), and reverse electrodialysis.[1, 4] Numerous strategies have been adopted to modify the substrates, such as minimizing the tortuosity and thickness, enhancing

porosity,[1, 12] improving hydrophilicity,[13, 14] using electrospun nanofibers[14, 15] or carbon nanotubes,[16] and adding a barrier layer.[17, 18] However, the resulting membranes with thin, highly porous supports are still subject to the ICP and particularly fouling. Additionally, thin and highly porous supports might not provide the necessary mechanical properties. Membranes based on 2D materials such as GO or MoS_2 nanosheets have also been explored,[11, 19, 20] and there remains challenge to fabricate the defect-free membranes at large scale. Recently, support-free symmetric nonporous membranes have been explored for FO[7, 21-25] and PRO applications.[26] This new platform of membranes is insusceptible to the ICP caused by the salts and foulants because they do not have porous substrates (cf. Figure 1a).

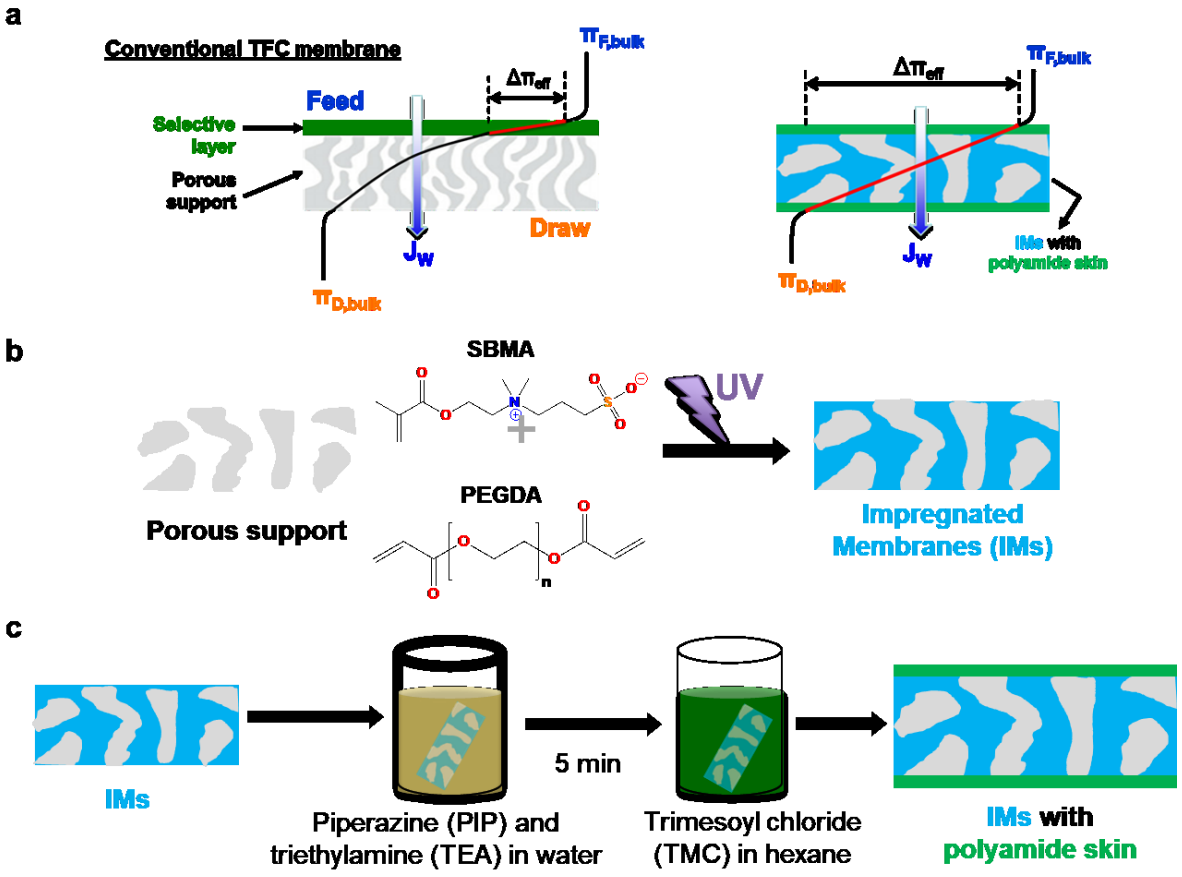

Figure 1. (a) Comparison of the effect of ICP on the apparent driving force in FO (*i.e.*, $\Delta\pi_{eff}$) between a conventional TFC membrane and a support-free membrane. Schematic of preparation of (b) IMs by photopolymerization[7] and (c) formation of the polyamide skin via the GLIP.

Figure 1b shows an example nonporous membrane for FO applications without ICP effect, hydrogel-impregnated membranes (IMs).[7] A thin porous membrane was impregnated with a prepolymer solution containing poly(ethylene glycol) diacrylate (PEGDA, MW = 700 g/mol), which was then photopolymerized to form hydrophilic hydrogels. The porous membrane provides mechanical strength, and the hydrogel offers the water/salt separation properties. While these IMs demonstrated a negligible effect of the ICP during the FO operation, their water permeance and salt rejection are lower than the state-of-the-art FO membranes, such as HTI OsMem TFC-ES (HTI). For example, HTI showed water permeance (A_w) of 0.23 liter m^{-2} h^{-1} bar^{-1} (LMH/bar) and NaCl rejection of 98.9%, and an IM derived from a prepolymer solution containing 60 wt.% PEGDA showed the A_w of 0.077 LMH/bar and NaCl rejection of 96.8%. Decreasing the PEGDA content in the prepolymer solution to 40 wt.% increased the A_w to 0.10 LMH/bar but decreased the rejection to 65.5%.[7]

Herein we demonstrate two effective approaches to collectively improve the water/salt separation properties of the IMs. First, the hydrogel surface can be modified with a highly selective polyamide (PA) layer by gel-liquid interfacial polymerization (GLIP).[27, 28] As shown in Figure 1c, the hydrogel can be immersed in the piperazine (PIP) aqueous solution and then exposed to trimesoyl chloride (TMC) in hexane. The resulting PA has been widely used for nanofiltration for water/salt separation. The addition of such skin to the IMs increases salt rejection without significantly decreasing water permeance. Second, zwitterionic hydrogels are prepared from PEGDA and sulfobetaine methacrylate (SBMA). The introduction of the SBMA increases the water permeability and water/salt selectivity.[29-31] The effect of the hydrogel composition, GLIP

conditions, and porous support properties on the water/salt separation properties is systematically investigated. Their FO performance is compared with state-of-the-art commercial FO membranes.

2. RESULTS AND DISCUSSION

2.1. Structure and properties of the PA-modified IMs

The PEGDA-derived IMs are denoted as *s*IM*x* or *p*IM*x* for those prepared from porous hydrophobic Solupor or hydrophilic polytetrafluoroethylene (*h*PTFE) support, respectively. The *x* represents the concentration of PEGDA in the prepolymer solution. The zwitterionic hydrogels based IMs are denoted as IMZ. The SBMA content in the PEGDA-*co*-SBMA is chosen to be 33.3 wt.% because a further increase in the SBMA content does not significantly enhance the water permeability or water/salt selectivity.[29, 31] The IMs modified with PA layers are denoted as IMZ*x*-NF*y*, where *y* is the w/v% of piperazine (PIP) in the aqueous solution. NF is used because PIP and TMC are often used to prepare nanofiltration (NF) membranes.

Figure 2a compares the FTIR spectra of the *h*PTFE support, a prepolymer solution containing PEGDA and SBMA, and *p*IMZ20-NF2 to understand the conversion of (meth)acrylate groups in SBMA and PEGDA. The porous support shows characteristic peaks of PTFE (1150 and 1205 cm^{-1}). The prepolymer solution exhibits three characteristic peaks of (meth)acrylate groups at 810, 1410, and 1640 cm^{-1},[29, 32] which disappear in the spectrum of *p*IMZ20-NF2, indicating the almost complete conversion of the (meth)acrylate after polymerization.

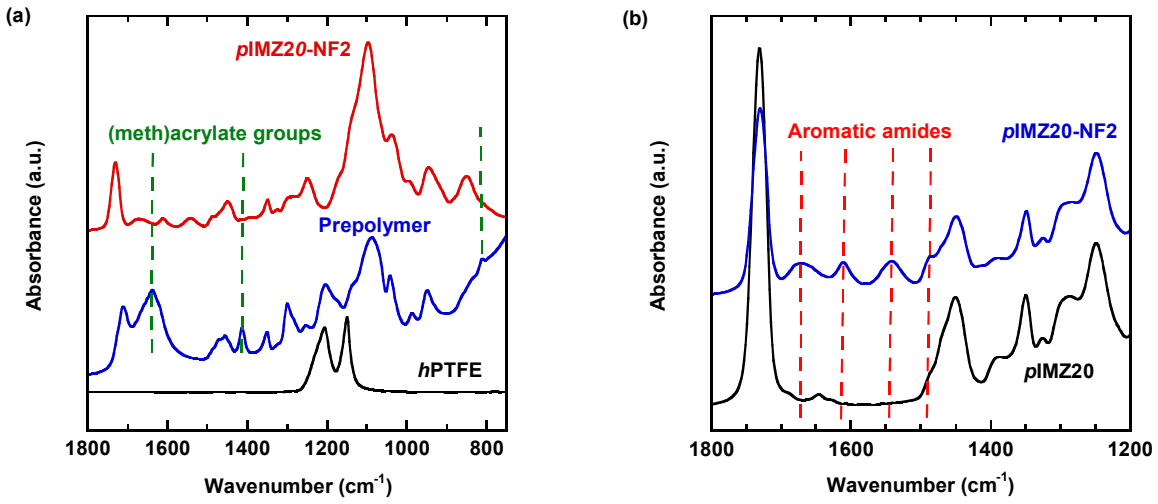

Figure 2. Comparison of FTIR spectra of (a) the *h*PTFE support, an aqueous prepolymer solution containing 20 wt.% PEGDA and 10 wt.% SBMA, and *p*IMZ20-NF2 for (meth)acrylate groups, and (b) *p*IMZ20 and *p*IMZ20-NF2 for aromatic amide groups.

Figure 2b compares the FTIR spectra of *p*IMZ20 and *p*IMZ20-NF2 to validate the formation of the PA layer. The appearance of the characteristic peaks of amide groups (at 1550, 1610, and 1680 cm^{-1})[24, 33, 34] and aromatic groups (at 1485 cm^{-1})[33] in *p*IMZ20-NF2 confirms the successful formation of the PA skin. Table S1 in the Supporting Information also shows that the water contact angle increases with the PA layer formation, consistent with the more hydrophobic nature of the PA than the hydrogels.

The surface topology and cross-section of the IMs were investigated using SEM. Figures 3a-c compare the surface topology of *h*PTFE, *p*IMZ20, and *p*IMZ20-NF2. The *h*PTFE support exhibits a porous structure, while the *p*IMZ20 shows a smooth surface because of the hydrogel. On the other hand, the *p*IMZ20-NF2 shows wrinkle features, consistent with the PA from the interfacial polymerization for the NF membranes.[24, 27] The large features on the surface were caused by the residual aqueous droplets, which were not completely removed before immersion into the TMC solution for the interfacial polymerization.

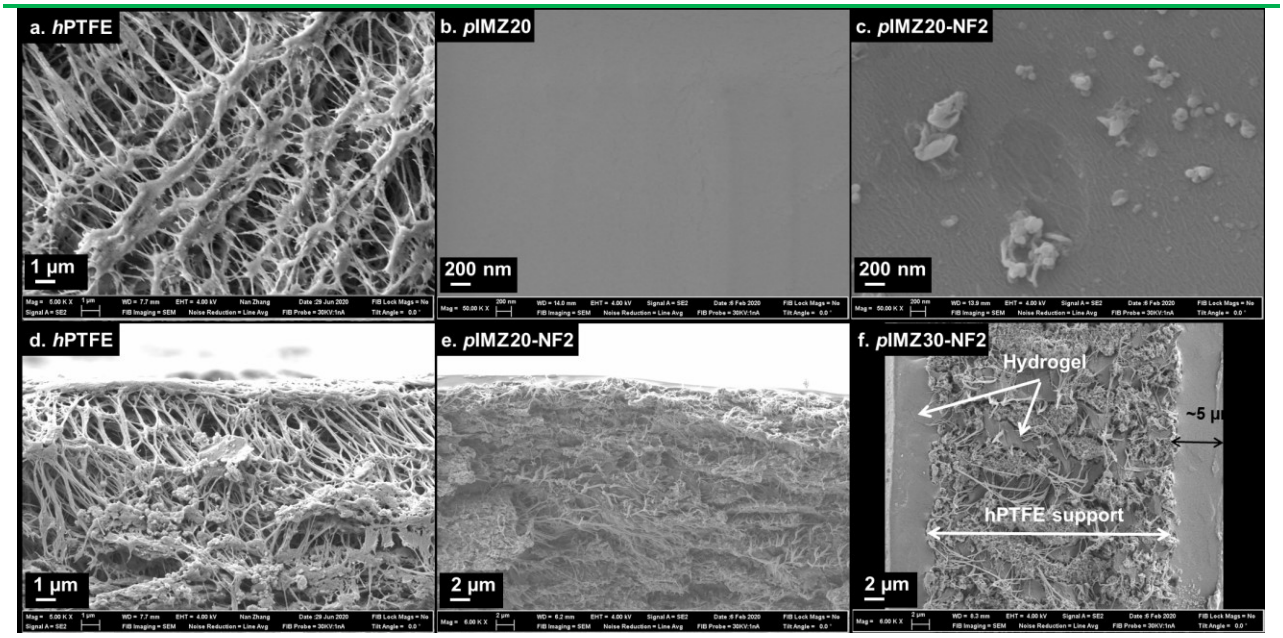

Figure 3. Comparison of the surface SEM images of (a) *h*PTFE, (b) IMZ20, and (c) *p*IMZ20-NF2. Comparison of the cross-sectional SEM images of (d) *h*PTFE, (e) *p*IMZ20-NF2, and (f) *p*IMZ30-NF2.

Figures 3d-f compare the cross-sectional images of *h*PTFE, *p*IMZ20-NF2, and *p*IMZ30-NF2. In both *p*IMZ20-NF2 and *p*IMZ30-NF2 samples, the porous *h*PTFE support was fully filled with the hydrogel due to the compatibility between the solution and support. The PEGDA content in the prepolymer solution seems to affect the thickness of the hydrogel layers on top of the porous support. For example, as the PEGDA content increases from 20 wt.% to 30 wt.%, the hydrogel thickness on top of the support increases from ≈ 2 µm to ≈ 5 µm. However, it is impossible to distinguish the PA layer from the hydrogel films presumably because of the strong adhesion.[24] Additionally, the PA layer is expected to be thinner than 0.25 µm due to the short reaction time of 5 min. For example, the PA layer has a thickness of ~ 0.25 µm when formed from *m*-phenylene diamine (MPD) and TMC on cross-linked poly(2-hydroxyethyl methacrylate) (PHEMA) in the GLIP process for 5 min.[24]

The surface roughness and nanomechanical properties of the PA-modified IMs were investigated by atomic force microscopy (AFM). The formation of the PA skin increases the surface roughness from 4.9 nm to 215 nm (cf. Figures 4a and 4b), and the surface modulus from 118 MPa to 1.0 GPa (cf. Figures 4c and 4d). Note that a larger scan size is used for Figure 4b to illustrate the long-range surface wrinkles. Accordingly, Figure 4d is taken from a ridge of the wrinkle in Figure 4b to minimize the effect of surface topography on modulus measurements. These changes are consistent with the PA formation on hydrogels[24, 27] or porous supports.[35]

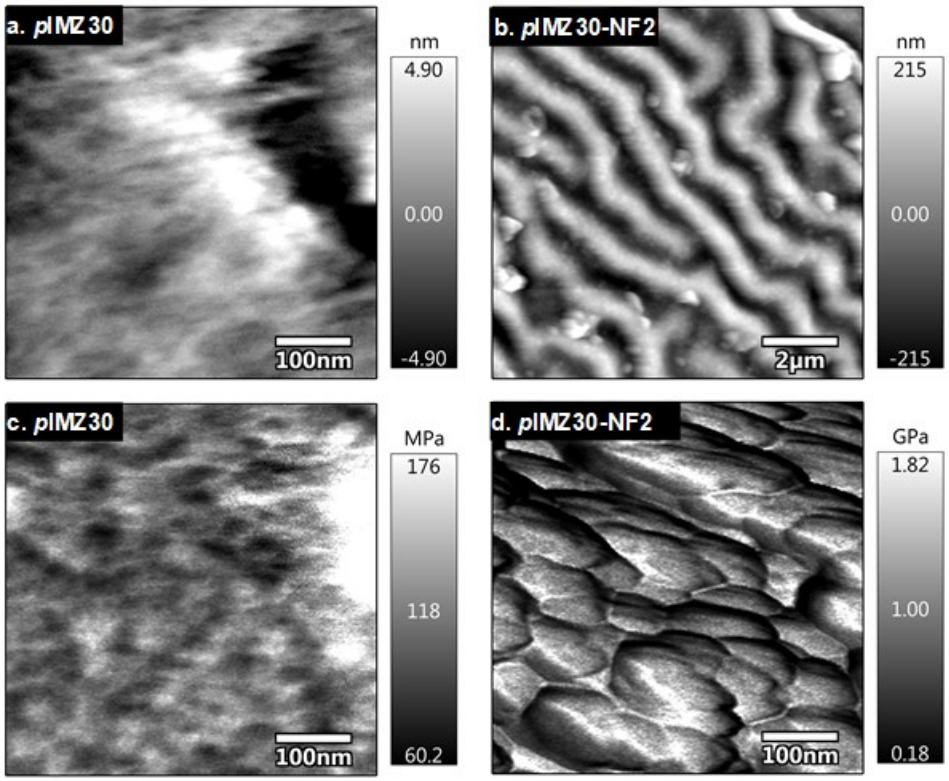

Figure 4. Comparison of the surface roughness of (a) *p*IMZ30 and (b) *p*IMZ30-NF2. Comparison of the surface modulus of (c) *p*IMZ30 and (d) *p*IMZ30-NF2.

2.2. Water and salt transport properties

Two porous supports were used in this study to demonstrate the versatility of our approach, including hydrophobic Solupor and hydrophilic *h*PTFE. The *s*IM30 and *p*IM30 were prepared

using the solvent of ethanol and water to ensure good wettability, respectively. The *p*IM30 shows pure-water permeance of 0.18 ± 0.05 LMH/bar, slightly higher than *s*IM30 (0.14 ± 0.03 LMH/bar), partially because *h*PTFE (*i.e.*, 35 μm) is 12% thinner than Solupor (*i.e.*, 40 μm). The comparison confirms that the change of the support does not significantly affect the IM properties.

Figure 5 presents the effect of the PEGDA concentration in the prepolymer solutions on A_W and the Na_2SO_4 rejection (R_S) in *s*IM*x* samples. Increasing the PEGDA concentration in the prepolymer solution from 20 wt.% to 40 wt.% decreases the A_W of the IMs from 0.5 ± 0.1 LMH/bar to 0.03 ± 0.01 LMH/bar but increases the Na_2SO_4 rejection from 22% ± 7% to 97% ± 2%, which can be ascribed to the increased cross-linking density.[32, 36, 37]

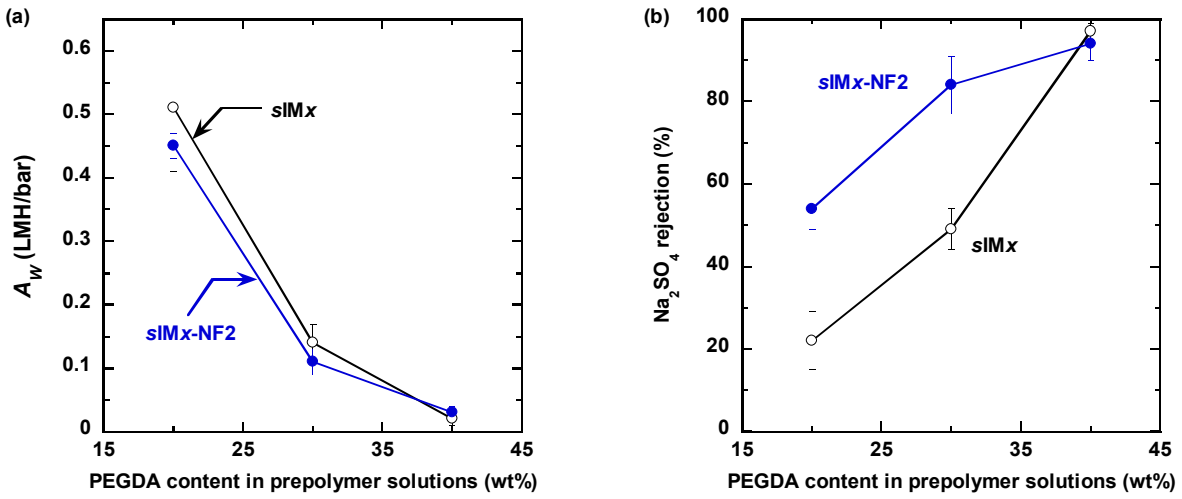

Figure 5. Effect of the PEGDA content in the prepolymer solutions on (a) A_W and (b) Na_2SO_4 rejection for the *s*IM*x* and *s*IM*x*-NF2. The Na_2SO_4 rejection was determined with 2 g/L Na_2SO_4 solution at 15 bar in dead-end permeation cells at ≈ 22 °C. The error bar represents one standard deviation of three samples.

The addition of the PA skin has a negligible effect on the A_w (cf. Figure 5a) but increases the Na_2SO_4 rejection (cf. Figure 5b) for *s*IM20 and *s*IM30. For example, *s*IM30 shows A_W of 0.14 ± 0.03 LMH/bar and Na_2SO_4 rejection of only 49% ± 10%, while *s*IM30-NF2 exhibits A_W of 0.11

± 0.02 LMH/bar and Na_2SO_4 rejection of 84% ± 7%. The IM30 samples have a balanced A_W and Na_2SO_4 rejection, and thus, they are chosen for further FO studies.

The introduction of the zwitterionic SBMA into the PEGDA-derived hydrogels has been demonstrated to improve hydrophilicity, water permeance, and water/NaCl selectivity.[29, 31] For example, as the SBMA content increased from 0 to 50 wt.% in the PEGDA-*co*-SBMA copolymers, water permeability increased from 1.4×10^{-5} cm^2/s to 8.4×10^{-5} cm^2/s, and water/NaCl selectivity increased from 38 to 52 despite the decreased cross-linking density.[29] However, it is difficult to dissolve SBMA into the prepolymer solution containing EtOH and PEGDA. Therefore, water was chosen as an alternative solvent, and the hydrophilic *h*PTFE was selected.[7]

Table 1 demonstrates the effect of the IM configurations on the A_w determined under the RO mode. The *p*IMZ20 is compared with *p*IM30 to elucidate the benefits of introducing SBMA in the hydrogels, as both have the same monomer content (30 wt.%) in the prepolymer solutions. The *p*IMZ20 exhibits slightly higher A_w (0.22 ± 0.07 LMH/bar) than *p*IM30 (0.18 ± 0.05 LMH/bar) due to the greater hydrophilicity and lower cross-linking density in *p*IMZ20 derived from the SBMA.[10, 29, 32, 38] The A_w of *p*IM30 is slightly higher than that of *s*IM30, presumably due to the thinner *h*PTFE support than the Solupor support, as both supports have similarly high porosity (≈ 84%) and large pores (~ 1 μm). The PA skins on both *p*IM30 and *p*IMZ20 slightly decrease A_W, but the changes are within the uncertainty.

The water permeance during the FO operation ($A_{w,FO}$) is usually lower than the A_w in RO operation due to the ICP. Na_2SO_4 solutions are used as the draw solutions, as the FO can be integrated with the NF for the draw solution recovery,[39, 40] and thus, they have been widely studied.[21, 23, 24] The performance ratio (defined as the ratio of $A_{w,FO}$ to A_w) can be used to determine the effect of ICP.[7] The higher the performance ratio is, the less susceptible the membrane is to the

CP. All of the IMs exhibit a performance ratio of 0.5 or higher. By contrast, the commercial NF90 membrane (TFC membranes consisting of a PA selective layer for water/Na_2SO_4 separation) exhibits a performance ratio of only 0.007, indicating a 99.3% loss in the driving force caused by the CP. Additionally, the $A_{w,FO}$ of the IMs is higher than that of typical TFC membranes such as NF90 and SW30-XLE. The state-of-the-art commercial FO membranes such as HTI and Aquaporin exhibit the performance ratio lower than those of IMs due to the high porosity of the HTI membrane (*i.e.*, 64%) and the porous substrate of the Aquaporin membrane.[5, 41] The $A_{w,FO}$ of *p*IM30-NF1.5 (0.12 ± 0.05 LMH/bar) and *p*IMZ20-NF1.5 (0.16 ± 0.03 LMH/bar) are comparable with the HTI (0.17 LMH/bar) and Aquaporin (0.20 LMH/bar), though their reverse salt flux (RSF) values are higher than those of commercial FO membranes.

Table 1. Water Permeance (A_W) and Reverse Salt Flux (RSF) during FO Operation Compared with the A_W in RO Mode.

Samples	A_w in FO[a] (LMH/bar)	RSF in FO (gMH)	A_w in RO[b] (LMH/bar)	Performance ratio
*p*IM30	0.16 ± 0.03	325 ± 45	0.18 ± 0.05	0.89 ± 0.09
*p*IM30-NF1.5	0.12 ± 0.05	16 ± 5	0.14 ± 0.03	0.9 ± 0.1
*p*IM30-NF2	0.14 ± 0.05	21 ± 7	0.15 ± 0.03	0.93 ± 0.07
*p*IMZ20	0.14 ± 0.05	155 ± 17	0.22 ± 0.07	0.67 ± 0.05
*p*IMZ20-NF1.5	0.16 ± 0.03[c]	18 ± 4[c]	0.20 ± 0.07	0.83 ± 0.15[c]
*p*IMZ20-NF2	0.13 ± 0.04[c]	12 ± 2[c]	0.18 ± 0.05	0.74 ± 0.02[c]
NF90	0.10 ± 0.03[c]	≈ 0	13 ± 1	0.007 ± 0.002[c]
SW30-XLE	0.05 ± 0.01	≈ 0	0.8 ± 0.3	0.06 ± 0.01
Aquaporin	0.20 ± 0.03	9.4 ± 0.7	3.2 ± 0.8	0.06 ± 0.03
HTI	0.17 ± 0.04	0.9 ± 0.1	0.53 ± 0.05	0.32 ± 0.04

[a] The feed and draw solution are DI water and 1M Na_2SO_4, respectively.
[b] Determined using pure-water and dead-end permeation cells at 15 bar.
[c] The uncertainty was estimated by the error propagation method.[42]

Similar to the A_w, the PA skin has a negligible effect on $A_{w,FO}$. For example, *p*IM30 exhibits an $A_{w,FO}$ value of 0.16 ± 0.03 LMH/bar, while *p*IM30-NF1.5 and *p*IM30-NF2 show the $A_{w,FO}$ value of 0.12 ± 0.05 LMH/bar and 0.14 ± 0.05 LMH/bar, respectively. The difference in these values is within the uncertainty. Similar results have been observed for *p*IMZ20 and its PA-modified samples. By contrast, the addition of the PA skin significantly reduces the RSF.[43] For example, *p*IM30-NF2 and *p*IM30-NF1.5 exhibit an RSF value of 21 ± 7 g m^{-2} h^{-1} (gMH) and 16 ± 5 gMH, respectively, much lower than the *p*IM30 (325 ± 45 gMH). For the *p*IMZ20 series, the RSF also reduces from 155 ± 17 gMH in *p*IMZ20 to 18 ± 4 gMH in *p*IMZ20-NF1.5 and 12 ± 2 gMH in *p*IMZ20-NF2. Similarly, when the PA is prepared using TMC and *m*-phenylenediamine (MPD), the salt rejection also increases (cf. Figure S1 and Table S1).

Table 1 also confirms that the introduction of the SBMA in the hydrogels increases the salt rejection in the FO operation.[10, 29, 31] Specifically, the RSF reduces by 52% from 325 gMH for *p*IM30 to 155 gMH for *p*IMZ20, though *p*IMZ20 has lower cross-linking density than *p*IM30. On the other hand, the *p*IMZ20 shows $A_{w,FO}$ only 12% lower than *p*IM30, increasing the water/salt selectivity. The flux selectivity for water over Na_2SO_4 (defined as the ratio of $A_{w,FO}$ to RSF) decreases from 48 in *p*IMZ20 to 25 in the *p*IM30.

The water and salt permeance through the PA skin was estimated using the resistance-in-series model.[44, 45]

$$A_w = \left[\frac{1}{A_{w,HG}} + 2\frac{1}{A_{w,PA}}\right]^{-1} \quad (1)$$

where the subscripts of HG and PA indicate the permeance of the hydrogel layer and the PA skin, respectively. Similarly, the salt permeance, B (LMH), of the membranes can be described as follow:[44]

$$B = \left[\frac{1}{B_{HG}} + 2\frac{1}{B_{PA}}\right]^{-1} \quad (2)$$

The B value for each membrane was estimated using the salt rejection, R_S, and the measured A_w in RO mode:[44]

$$R_S = \frac{\left(A_W/B\right)(\Delta p - \Delta\pi)}{1 + \left(A_W/B\right)(\Delta p - \Delta\pi)} \times 100\% \quad (3)$$

where Δp (bar) is the transmembrane pressure, and $\Delta\pi$ (bar) is the difference of the osmotic pressure.

Table 2 presents the calculated A_w and B for each layer of the IMs using Equations 1-3. In all modified membranes, the $A_{w,PA}$ is greater than the $A_{w,HG}$, indicating a more significant resistance to water transport in the hydrogel layer than the PA skin. Therefore, the added PA skin has a negligible effect on the water permeance (cf. Figure 5 and Table 1). The PA skin in *p*IM30-NF1.5 shows $A_{w,PA}$ of 1.3 ± 0.3 LMH/bar, lower than that of *p*IMZ20-NF1.5 (4.4 ± 1.3 LMH/bar), suggesting that the PA skin of *p*IMZ20-NF1.5 is thinner than the *p*IM30-NF1.5 skin layer. On the other hand, both *p*IM30-NF2 and *p*IMZ20-NF2 demonstrate similar water permeance in the PA skin (≈ 2 LMH/bar).

Table 2. Water Permeance ($A_{W,i}$) and Salt Permeance (B_i) of the Hydrogel (i = HG) and Polyamide Skin (i = PA) in RO Mode.

Samples	$A_{w,HG}$ (LMH/bar)	$A_{w,PA}$ (LMH/bar)	B_{HG} (LMH)	B_{PA} (LMH)
*p*IM30	0.18 ± 0.05	n/a	5 ± 1	n/a
*p*IM30-NF1.5	0.18 ± 0.05	1.3 ± 0.3	5 ± 1	0.9 ± 0.3
*p*IM30-NF2	0.18 ± 0.05	1.8 ± 0.5	5 ± 1	1.7 ± 0.2
*p*IMZ20	0.22 ± 0.07	n/a	2.4 ± 0.6	n/a
*p*IMZ20-NF1.5	0.22 ± 0.07	4.4 ± 1.3	2.4 ± 0.6	1.3 ± 0.2
*p*IMZ20-NF2	0.22 ± 0.07	2.0 ± 0.6	2.4 ± 0.6	0.65 ± 0.04

*Note: the uncertainty is estimated using the error propagation method.[42]

The *p*IMZ20 series exhibit much lower B_{HG} values than the *p*IM30, confirming that the introduction of zwitterions increases the resistance to salt transport in the hydrogels. Moreover, the water/salt selectivity (*i.e.*, A_w/B) of the zwitterionic hydrogels is higher than that of PEGDA-hydrogels, consistent with the observed RSF results. For example, *p*IMZ20 shows an RSF of 155 gMH in the FO operation, significantly lower than *p*IM30 (325 gMH). Additionally, the lower B_{PA} values than the B_{HG} values signify that the PA skin exhibits greater resistance to salt transport than the hydrogels.

2.3. FO performance under fouling conditions

Figure 6 compares the water flux of *p*IMZ20-NF1.5 and HTI membranes under the FO mode with 1 g/L bovine serum albumin (BSA) as the feed for 24-h continuous operation. Both membranes demonstrated similar initial $A_{w,FO}$ of ≈ 0.17 LMH/bar or J_w of ≈ 8 LMH. However, the J_w of the HTI membrane decreases quickly while J_w of *p*IMZ20-NF1.5 remains relatively constant. Over the 24-h period, the *p*IMZ20-NF1.5 shows the J_w 25% higher than the HTI membrane, suggesting that the *p*IMZ20-NF1.5 is more resistant to fouling. This evaluation also demonstrates the stability of *p*IMZ20-NF1.5 under the 24-h continuous operation.

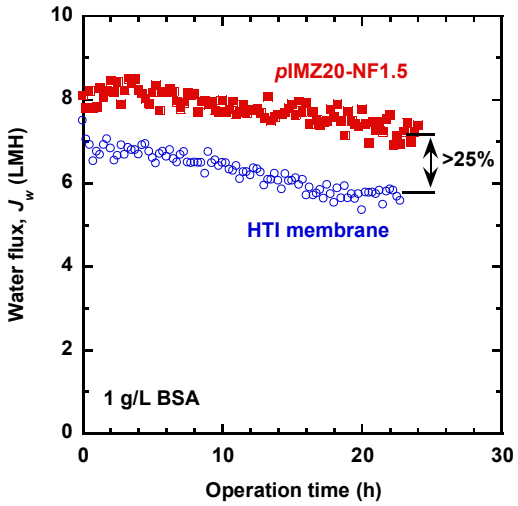

Figure 6. Comparison of the FO water flux of pIMZ20-NF1.5 and HTI membranes for 24-h continuous operation. The feed contains 1 g/L BSA at ≈1.5 L/min, while the draw solution is 1 M Na_2SO_4 at ≈1.5 L/min.

We have also tested the stability of the *p*IMZ20-NF1.5 for typical cleaning solutions. The samples were immersed in a 0.001 M HCl solution (pH = 3.0) or a 0.001 M NaOH solution (pH = 11) for 6 h. The samples maintain their integrity without any visible damages (cf. Figure S2).

3. CONCLUSIONS

We demonstrate a new membrane configuration of IMs with PA skin, which can exhibit water/salt separation properties for FO applications comparable with the state-of-the-art commercial membranes and improved fouling properties, despite the commercial membranes had been optimized for almost three decades. The porous membrane provides excellent mechanical strength, the zwitterionic hydrogels eliminate the pores and associated ICP, and the PA skin yields superior water/salt selectivity but a negligible resistance to water transport compared with the hydrogels. The formation of the PA skin significantly increases the surface roughness and modulus. The IMs exhibit a much higher performance ratio than the commercial membranes (*i.e.*, NF90, SW30-XLE, HTI, and Aquaporin), validating the mitigated ICP effect in the PA-augmented IMs.

The *p*IMZ20-NF1.5 demonstrates water permeance (≈ 0.2 LMH/bar) comparable to the state-of-the-art commercial FO membranes (such as HTI and Aquaporin) and better resistance to model foulants such as BSA. These results highlight the promise of this membrane configuration to design next-generation membranes for osmotic pressure-driven processes.

4. EXPERIMENTAL SECTION

Materials. Solupor (with a thickness of 45 μm, a pore size of 0.7 μm, and a porosity of 84%) and *h*PTFE (with a thickness of 35 μm, a pore size of 1.0 μm, and a porosity of 83%) were purchased from Lydall Performance Materials, Inc. (Rochester, NH) and Advantec MFS, Inc. (Dublin, CA), respectively. FO membranes of Aquaporin and HTI were procured from Aquaporin A/S (Lyngby, Denmark) and Fluid Technology Solutions (Albany, OR, USA), respectively. NF90 and SW30-XLE RO membranes were purchased from Sterlitech (Kent, WA). PEGDA (Mn =700 g/mol), SBMA, PIP, TMC, TEA, HCPK, and BSA were provided by Sigma-Aldrich Chemical (Milwaukee, WI). Ethanol (95%), *n*-hexane, sodium sulfate, sodium chloride, sodium hydroxide, and 2 N hydrochloric acid solution were purchased from Thermo Fisher Scientific Co. (Hampton, NH). Deionized water was generated by Milli-Q Ultrapure Water System (18.2 MΩ/cm at 23.8 °C) (EMD Millipore, Billerica, MA).

Preparation of IMs. The IMs were prepared using the following procedures.[7] First, a prepolymer solution was prepared by dissolving a desirable amount of PEGDA in water or ethanol. Water and ethanol were used as the solvent for the *h*PTFE and Solupor support, respectively, to ensure that the support can be wet by the solution. Second, SBMA (10 wt.%) and HCPK (0.1 wt.% relative to the PEGDA) were added to the solution. Third, a 3-inch-by-5-inch support sample was coated twice on each side with the solution using a foam brush. The sample was then sandwiched

between two quartz plates and exposed to 254-nm UV light for 5 min in a UV crosslinker (UVP Model CX-2000, Thermo Fisher Scientific) for the monomers to photopolymerize. Finally, the IM sample was removed from the plates and stored in DI water for 24 h until further use.

The PA skin on the IMs was prepared using the GLIP with the following example procedures.[24, 27] First, an IM sample was immersed in a solution containing 1.5 or 2.0 w/v% PIP (g per 100 mL water) and the same content of TEA for 24 h. The sample was then taken out, and the excess solution on the surface was removed using filter paper. Second, the sample was immersed in a hexane solution containing TMC for 5 min for interfacial polymerization, where the concentration ratio of TMC to PIP is 1:20. The membrane was then washed with hexane to remove the unreacted monomers before drying in the air for 1 min and in an oven at 50 ℃ for 5 min. Finally, the membrane was stored in DI water before uses.

Characterization of the IMs. Before any characterization, the IMs were dried in a vacuum oven at 60°C for 24 h. The membranes were characterized using ATR-FTIR spectroscopy (Bruker Vertex 70, Billerica, MA) to confirm the conversion of meth(acrylate) groups in PEGDA and SBMA and the formation of PA skin after the GLIP. The membrane surface and cross-section were imaged using SEM (AURIGA CrossBeam, Germany). The surface topography and modulus of the coating layers were investigated by AFM (Cypher, Asylum Research) in Fast Force Mapping (FFM) mode with a 7.4 N/m force constant tip (All in One-Al, Budget Sensors). The FFM measurement provides a rapid mapping of the spatially resolved surface modulus of the membranes. The FFM data was fit to a Hertz contact mechanics model to obtain modulus values, using tip radius calibrated using standard glassy polystyrene sample.

The A_w (LMH/bar) was determined using dead-end filtration cells and calculated using the equation below:[7, 45]

$$A_W = \frac{J_W}{\Delta p} = \frac{V}{t \Delta p A_m} \quad (4)$$

where A_m is the active membrane area (m^2), and V is the volume of the water permeated (L) over the time of t (h).

The rejection for Na_2SO_4 (R_S) was determined using dead-end filtration cells and calculated using Equation 5:[7, 45]

$$R_S = (1 - C_P / C_F) \times 100\% \quad (5)$$

where C_P and C_F are the salt concentration in the permeate and feed, respectively. The C_P and C_F were determined using a conductivity meter (CON-BTA, Vernier Software and Technology, Beaverton, OR) and a predetermined calibration curve for each salt. The C_F is ≈2000 ppm.

The FO performance of the membranes was determined using a custom-built system operating in counter-current mode.[7, 8, 43] The feed and draw solution was DI water and 1 M Na_2SO_4 solution (or 142 g/L), respectively. Both solutions had a flow rate of 83 L/h at atmospheric pressure. The mass of feed and draw reservoirs was continuously monitored using digital balances. Water flux can be calculated based on the mass decrease (Δm_F, g) of the feed solution or the mass increase of the draw solutions (Δm_D) at time t (h) relative to $t = 0$. The $A_{W,FO}$ can be calculated based on the average of the two mass changes using Equation 6:

$$A_{W,FO} = \frac{\Delta m_F + \Delta m_D}{2 \rho_W t A_m (\pi_D - \pi_F)} \quad (6)$$

where ρ_W is water density (1000 g/L). The subscripts of D and F represent the draw and feed solution, respectively. The osmosis pressure is calculated using the following equation:

$$\pi_i = n \Phi C_i R T \quad (7)$$

where n is the number of ions (3 for Na_2SO_4), Φ is the osmotic coefficient (0.74 for Na_2SO_4), R is the gas constant (0.08314 L·bar K^{-1}·mol^{-1}), and T is the absolute temperature (295 K in this study).

The reverse salt flux (J_S, gMH) can be calculated using Equation 8:[43]

$$J_S = \frac{C_F V_F}{t A_m} \quad (8)$$

where V_F (L) is the feed solution volume at time t.

The membrane antifouling properties during FO were evaluated using 1 g/L BSA in PBS buffer solution (pH = 7.4) as the feed and 1 M Na_2SO_4 as the draw solution for 24 h.

■ ASSOCIATED CONTENT

Supporting Information

The Supporting Information is available free of charge on the ACS Publications website.

Preparation and characterization of the *s*IM*x* samples with the polyamide derived from TMC and MPD.

■ AUTHOR INFORMATION

Corresponding Author

*E-mail: haiqingl@buffalo.edu (H. Lin)

ORCID

Yifu Ding: 0000-0001-7779-7781

Haiqing Lin: 0000-0001-8042-154X

Author Contributions

The manuscript was prepared through the contributions of all authors. All authors have approved the final version of the manuscript.

Notes

The authors declare no competing financial interest.

■ ACKNOWLEDGMENTS

We acknowledge the financial support from the U.S. National Science Foundation (NSF) with Award No. 1635026 and the U.S. Department of Interior with Award No. R17AC00147.

■ REFERENCES

1. Suwaileh, W.; Pathak, N.; Shon, H.; Hilal, N., Forward Osmosis Membranes and Processes: A Comprehensive Review of Research Trends and Future Outlook, *Desalination* **2020,** *485*, 114455.

2. Shaffer, D. L.; Werber, J. R.; Jaramillo, H.; Lin, S.; Elimelech, M., Forward Osmosis: Where Are We Now?, *Desalination* **2015,** *356*, 271-284.

3. Chung, T.; Luo, L.; Wan, C.; Cui, Y.; Amy, G., What is Next for Forward Osmosis (FO) and Pressure Retarded Osmosis (PRO), *Sep. Purif. Technol.* **2015,** *156*, 856-860.

4. Straub, A. P.; Deshmukh, A.; Elimelech, M., Pressure-retarded Osmosis for Power Generation from Salinity Gradients: Is It Viable?, *Energy Environ. Sci.* **2016,** *9* (1), 31-48.

5. Dutta, S.; Nath, K., Feasibility of Forward Osmosis Using Ultra Low Pressure RO Membrane and Glauber Salt as Draw Solute for Wastewater Treatment, *J. Environ. Chem. Eng.* **2018,** *6* (4), 5635-5644.

6. McCutcheon, J. R.; Elimelech, M., Influence of Concentrative and Dilutive Internal Concentration Polarization on Flux Behavior in Forward Osmosis, *J. Membr. Sci.* **2006,** *284* (1-2), 237-247.

7. Zhao, S.; Huang, K.; Lin, H., Impregnated Membranes for Water Purification Using Forward Osmosis, *Ind. Eng. Chem. Res.* **2015,** *54* (49), 12354-12366.

8. Xu, J.; Tran, T. N.; Lin, H.; Dai, N., Removal of Disinfection Byproducts in Forward Osmosis for Wastewater Recycling, *J. Membr. Sci.* **2018,** *564*, 352-360.

9. She, Q.; Wang, R.; Fane, A. G.; Tang, C., Membrane Fouling in Osmotically Driven Membrane Processes: A Review, *J. Membr. Sci.* **2016,** *499*, 201-233.

10. Firouzjaei, M. D.; Seyedpour, S. F.; Aktij, S. A.; Giagnorio, M.; Bazrafshan, N.; Mollahosseini, A.; Samadi, F.; Ahmadalipour, S.; Firouzjaei, F. D.; Esfahani, M. R.; Tiraferri, A.; Elliott, M.; Sangermano, M.; Abdelrasoul, A.; McCutcheon, J. R.; Sadrzadeh, M.; Esfahani, A. R.; Rahimpour, A., Recent Advances in Functionalized Polymer Membranes for Biofouling Control and Mitigation in Forward Osmosis, *J. Membr. Sci.* **2020,** *596*, 117604.

11. Hu, M.; Zheng, S.; Mi, B., Organic Fouling of Graphene Oxide Membranes and Its Implications for Membrane Fouling Control in Engineered Osmosis, *Environ. Sci. Technol.* **2016,** *50* (2), 685-693.

12. Manickam, S. S.; McCutcheon, J. R., Understanding Mass Transfer Through Asymmetric Membranes during Forward Osmosis: A Historical Perspective and Critical Review on Measuring Structural Parameter with Semi-empirical Models and Characterization Approaches, *Desalination* **2017,** *421*, 110-126.

13. Arena, J. T.; McCloskey, B.; Freeman, B. D.; McCutcheon, J. R., Surface Modification of Thin Film Composite Membrane Support Layers with Polydopamine: Enabling Use of Reverse Osmosis Membranes in Pressure Retarded Osmosis, *J. Membr. Sci.* **2011,** *375* (1), 55-62.

14. Moon, S.; Kim, J.; Seong, J.; Lee, W.; Park, S.; Noh, S.; Kim, J.; Lee, Y., Thin Film Composite on Fluorinated Thermally Rearranged Polymer Nanofibrous Membrane Achieves Power Density of 87 W m^{-2} in Pressure Retarded Osmosis, Improving Economics of Osmotic Heat Engine, *J. Membr. Sci.* **2020,** *607*, 118120.

15. Song, X.; Liu, Z.; Sun, D. D., Nano Gives the Answer: Breaking the Bottleneck of Internal Concentration Polarization with a Nanofiber Composite Forward Osmosis Membrane for a High Water Production Rate, *Adv. Mater.* **2011,** *23* (29), 3256-3260.

16. Zhou, Z.; Hu, Y.; Wang, Q.; Mi, B., Carbon Nanotube-supported Polyamide Membrane with Minimized Internal Concentration Polarization for Both Aqueous and Organic Solvent Forward Osmosis Process, *J. Membr. Sci.* **2020,** *611*, 118273.

17. Han, G.; Cheng, Z.; Chung, T., Thin-film Composite (TFC) Hollow Fiber Membrane with Double-polyamide Active Layers for Internal Concentration Polarization and Fouling Mitigation in Osmotic Processes, *J. Membr. Sci.* **2017,** *523*, 497-504.

18. Fang, W.; Wang, R.; Chou, S. R.; Setiawan, L.; Fane, A. G., Composite Forward Osmosis Hollow Fiber Membranes: Integration of RO- and NF-like Selective Layers to Enhance Membrane Properties of Anti-scaling and Anti-internal Concentration Polarization, *J. Membr. Sci.* **2012,** *394*, 140-150.

19. Ries, L.; Petit, E.; Michel, T.; Diogo, C. C.; Gervais, C.; Salameh, C.; Bechelany, M.; Balme, S.; Miele, P.; Onofrio, N.; Voiry, D., Enhanced sieving from exfoliated MoS2 membranes via covalent functionalization, *Nature materials* **2019,** *18* (10), 1112-1117.

20. Huang, L.; Huang, S.; Venna, S. R.; Lin, H., Rightsizing Nanochannels in Reduced Graphene Oxide Membranes by Solvating for Dye Desalination, *Environ. Sci. Technol.* **2018,** *52* (21), 12649-12655.

21. Cheng, W.; Ma, J.; Zhang, X.; Elimelech, M., Sub-1 μm Free-standing Symmetric Membrane for Osmotic Separations, *Environ. Sci. Tech. Let.* **2019,** *6* (8), 492-498.

22. Phuntsho, S.; Kim, J. E.; Tran, V. H.; Tahara, S.; Uehara, N.; Maruko, N.; Matsuno, H.; Lim, S.; Shon, H. K., Free-standing, Thin-film, Symmetric Membranes: Next-generation Membranes for Engineered Osmosis, *J. Membr. Sci.* **2020,** *607*, 118145.

23. Li, M.; Karanikola, V.; Zhang, X.; Wang, L.; Elimelech, M., A Self-standing, Support-free Membrane for Forward Osmosis with No Internal Concentration Polarization, *Environ. Sci. Tech. Let.* **2018,** *5* (5), 266-271.

24. Li, M.; Wang, X.; Porter, C. J.; Cheng, W.; Zhang, X.; Wang, L.; Elimelech, M., Concentration and Recovery of Dyes from Textile Wastewater Using A Self-standing, Support-free Forward Osmosis Membrane, *Environ. Sci. Technol.* **2019,** *53* (6), 3078-3086.

25. Liu, T.; Yuan, H.; Liu, Y.; Ren, D.; Su, Y.; Wang, X., Metal-organic Framework Nanocomposite Thin Films with Interfacial Bindings and Self-standing Robustness for High Water Flux and Enhanced Ion Selectivity, *ACS Nano* **2018,** *12* (9), 9253-9265.

26. Ma, T.; Balanzat, E.; Janot, J. M.; Balme, S., Nanopore Functionalized by Highly Charged Hydrogels for Osmotic Energy Harvesting, *ACS Appl. Mater. Interfaces* **2019,** *11* (13), 12578-12585.

27. Wang, M.; Gorham, J. M.; Killgore, J. P.; Omidvar, M.; Lin, H.; DelRio, F. W.; Cox, L. M.; Zhang, Z.; Ding, Y., Formation of a Crack-free, Hybrid Skin Layer with Tunable Surface Topography and Improved Gas Permeation Selectivity on Elastomers Using Gel–Liquid Infiltration Polymerization, *ACS Appl. Mater. Interfaces* **2017,** *9* (33), 28100-28106.

28. Wang, M.; Stafford, C. M.; Cox, L. M.; Blevins, A. K.; Aghajani, M.; Killgore, J. P.; Ding, Y., Controlled Growth of Polyamide Films Atop Homogenous and Heterogeneous Hydrogels Using Gel–Liquid Interfacial Polymerization, *Macromol. Chem. Phys.* **2019,** *220* (13), 1900100.

29. Shah, S.; Liu, J.; Ng, S.; Luo, S.; Guo, R.; Cheng, C.; Lin, H., Transport Properties of Small Molecules in Zwitterionic Polymers, *J. Polym. Sci., Part B: Polym. Phys.* **2016,** *54* (19), 1924-1934.

30. Tran, T.; Lin, C.; Chaurasia, S.; Lin, H., Elucidating the Relationship Between States of Water and Ion Transport Properties in Hydrated Polymers, *J. Membr. Sci.* **2019,** *574*, 299-308.

31. Ni, L.; Meng, J.; Geise, G. M.; Zhang, Y.; Zhou, J., Water and Salt Transport Properties of Zwitterionic Polymers Film, *J. Membr. Sci.* **2015,** *491*, 73-81.

32. Lin, H.; Kai, T.; Freeman, B. D.; Kalakkunnath, S.; Kalika, D. S., The Effect of Cross-linking on Gas Permeability in Cross-linked Poly(ethylene glycol diacrylate), *Macromolecules* **2005,** *38* (20), 8381-8393.

33. Zimudzi, T. J.; Feldman, K. E.; Sturnfield, J. F.; Roy, A.; Hickner, M. A.; Stafford, C. M., Quantifying Carboxylic Acid Concentration in Model Polyamide Desalination Membranes via Fourier Transform Infrared Spectroscopy, *Macromolecules* **2018,** *51* (17), 6623-6629.

34. Tang, C.; Kwon, Y.; Leckie, J. O., Effect of Membrane Chemistry and Coating Layer on Physiochemical Properties of Thin Film Composite Polyamide RO and NF Membranes I. FTIR and XPS Characterization of Polyamide and Coating Layer Chemistry, *Desalination* **2009,** *242* (1-3), 149-167.

35. Tang, C.; Kwon, Y.; Leckie, J. O., Effect of Membrane Chemistry and Coating Layer on Physiochemical Properties of Thin Film Composite Polyamide RO and NF Membranes II. Membrane Physiochemical Properties and Their Dependence on Polyamide and Coating Layers, *Desalination* **2009,** *242* (1-3), 168-182.

36. Yan, N.; Paul, D. R.; Freeman, B. D., Water and Ion Sorption in A Series of Cross-linked AMPS/PEGDA Hydrogel Membranes, *Polymer* **2018,** *146*, 196-208.

37. Tran, T. N.; Ramanan, S. N.; Lin, H., Synthesis of Hydrogels with Antifouling Properties as Membranes for Water Purification, *J. Vis. Exp.* **2017,** (122), e55426.

38. Kamcev, J.; Paul, D. R.; Manning, G. S.; Freeman, B. D., Predicting Salt Permeability Coefficients in Highly Swollen, Highly Charged Ion Exchange Membranes, *ACS Appl. Mater. Interfaces* **2017,** *9* (4), 4044-4056.

39. Giagnorio, M.; Ricceri, F.; Tiraferri, A., Desalination of Brackish Groundwater and Reuse of Wastewater by Forward Osmosis Coupled with Nanofiltration for Draw Solution Recovery, *Water Res.* **2019,** *153*, 134-143.

40. Giagnorio, M.; Ricceri, F.; Tagliabue, M.; Zaninetta, L.; Tiraferri, A., Hybrid Forward Osmosis–Nanofiltration for Wastewater Reuse: System Design, *Membranes* **2019,** *9* (5), 61.

41. Wei, J.; Qiu, C.; Tang, C.; Wang, R.; Fane, A. G., Synthesis and Characterization of Flat-sheet Thin Film Composite Forward Osmosis Membranes, *J. Membr. Sci.* **2011,** *372* (1), 292-302.

42. Bevington, P. R.; Robinson, D. K., *Data Reduction and Error Analysis for the Physical Sciences*. 2nd ed.; McGraw-Hill, Inc.: New York, 1992.

43. Xu, J.; Tran, T. N.; Lin, H.; Dai, N., Modeling the Transport of Neutral Disinfection Byproducts in Forward Osmosis: Roles of Reverse Salt Flux, *Water Res.* **2020,** *185*, 116225.

44. Sagle, A. C.; Van Wagner, E. M.; Ju, H.; McCloskey, B. D.; Freeman, B. D.; Sharma, M. M., PEG-coated Reverse Osmosis Membranes: Desalination Properties and Fouling Resistance, *J. Membr. Sci.* **2009,** *340* (1), 92-108.

45. Chen, X.; Feng, Z.; Gohil, J.; Stafford, C. M.; Dai, N.; Huang, L.; Lin, H., Reduced Holey Graphene Oxide Membranes for Desalination with Improved Water Permeance, *ACS Appl. Mater. Interfaces* **2020,** *12* (1), 1387-1394.

Table of Content Graphic